Geophysical Research Letters

RESEARCH LETTER
10.1029/2020GL088425

Bottom Drag Varies Seasonally With Biological Roughness

Galen Egan[1], Grace Chang[2], Gene Revelas[3], Stephen Monismith[1], and Oliver Fringer[1]

[1]Department of Civil and Environmental Engineering, Stanford University, Stanford, CA, USA, [2]Integral Consulting Inc., Santa Cruz, CA, USA, [3]Integral Consulting Inc., Olympia, WA, USA

Key Points:
- Measured drag coefficients vary across seasons, tidal cycles, and measurement devices
- Dense canopies of living roughness elements may increase drag
- Spatial/seasonal variations in benthic biology should be incorporated into drag parameterizations

Correspondence to:
G. Egan,
gegan@stanford.edu

Citation:
Egan, G., Chang, G., Revelas, G., Monismith, S., & Fringer, O. (2020). Bottom drag varies seasonally with biological roughness. *Geophysical Research Letters*, *47*, e2020GL088425. https://doi.org/10.1029/2020GL088425

Received 14 APR 2020
Accepted 9 JUL 2020
Accepted article online 17 JUL 2020

Abstract Over the course of a year, we conducted three field deployments in South San Francisco Bay to examine seasonal variability in bottom drag. Our data consisted of turbulence measurements both within and outside the bottom boundary layer and benthic characterization surveys adjacent to our study site. Our results suggest that canopies of benthic worm and amphipod feeding tubes, which were denser during summer, can increase the drag coefficient by up to a factor of three relative to the smoother beds found in winter and spring. The extent of the drag increase varied depending on the measurement device, with the greatest increase inferred by measurements taken further from the bed. The small scale and temporally varying population densities of these living roughness elements pose significant challenges for hydrodynamic models, and future work is needed to begin incorporating benthic biology statistics into drag coefficient parameterizations.

Plain Language Summary Tidal flows in estuaries are affected by the properties of the seafloor. By taking flow measurements in South San Francisco Bay during three different seasons, we show here that feeding tubes built by organisms that live in the sediment bed during summer make the bed much rougher and slow down average flow velocities. The extent of the estimated difference in roughness depends on the instrument used for the measurement, but the overall results imply that these bottom-dwelling populations should be taken into account when modeling flows in estuaries.

1. Introduction

In the absence of baroclinic pressure gradients, the 1-D, time-averaged momentum equation in estuaries can be approximated as a balance between the tidal pressure gradient and bottom friction (Geyer et al., 2000),

$$\frac{1}{\rho_0}\frac{\partial p}{\partial x} = \frac{\partial \tau_b}{\partial z}. \tag{1}$$

Here, ρ_0 is the fluid density, τ_b is the bottom shear stress, z is the vertical coordinate, and the pressure gradient, $\frac{\partial p}{\partial x}$, drives flow in the x-direction. The tidal pressure gradient can be estimated with reasonable accuracy (Egbert & Erofeeva, 2002; Pawlowicz et al., 2002), and the bottom stress τ_b is commonly parameterized with the quadratic drag law,

$$\tau_b = \rho_0 C_D \bar{u}|\bar{u}|, \tag{2}$$

where C_D is the drag coefficient and $\bar{u}$ is the mean near-bed velocity in the x-direction (Longuet-Higgins, 1970). Analytical models have been proposed that estimate the bottom drag as a function of bed roughness and wave conditions (Grant & Madsen, 1979; Styles & Glenn, 2000), though in practice the bottom roughness is not generally known with sufficient spatiotemporal resolution. Therefore, C_D is often estimated from in situ data or tuned to match observations (Fringer et al., 2019).

Numerous studies have examined variability in C_D with waves, tides, and bathymetry (for a review, see Trowbridge & Lentz, 2018). In this paper, we expand on that work by comparing drag measurements taken both within and outside the combined wave-current boundary layer in a shallow flow over a cohesive sediment bed. We show that variations in drag between tidal cycles and across seasons may be caused by spatially heterogeneous patches of biological roughness elements and comment on the implications for hydrodynamic modeling.

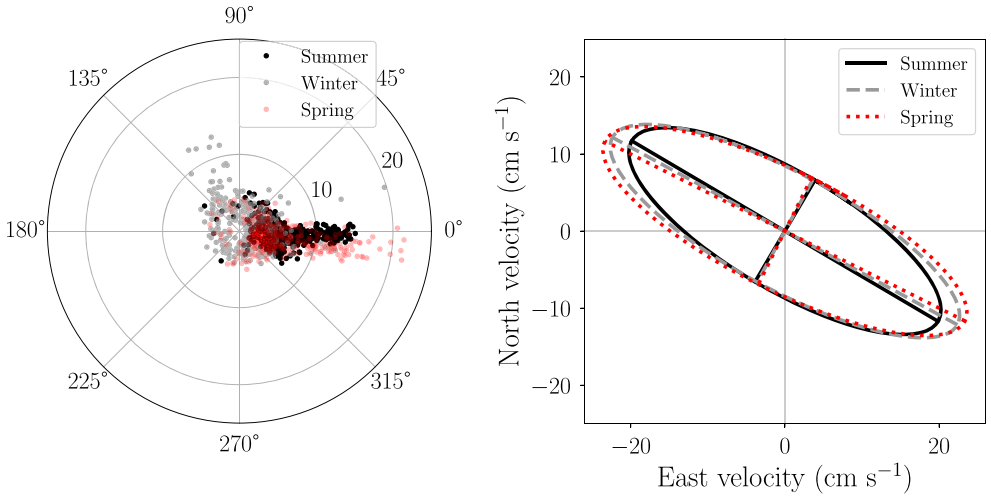

Figure 1. Left: Wave magnitude and direction from each measurement burst for all three deployments, with 0° corresponding to an eastward propagating wave, and the radial axis representing bottom wave-orbital velocity, u_b, in cm s^{-1}. Right: Tidal ellipses (propagating counterclockwise) for each of the three deployments, calculated from ADP velocity data depth-averaged below 100 cmab.

2. Field Work

Field work was conducted on the eastern shoals of South San Francisco Bay during 07/17/2018–08/15/2018 (summer deployment), 01/10/2019–02/07/2019 (winter deployment), and 04/17/2019–05/15/2019 (spring deployment). Our study site was situated at 1.5 m mean lower low water, with a tidal range of 2 m. Figure 1 depicts the wave conditions and tidal ellipses at the study site for all three deployments. Tidal current velocities depth-averaged over the bottom meter of the water column reached a maximum of approximately 28 cm s^{-1}, flowing southeast during flood tide and northwest during ebb tide. During summer and spring, diurnal northwesterly winds drove waves eastward each afternoon, with bottom wave-orbital velocities reaching 20 cm s^{-1}. Winter wave conditions were more subdued, with the exception of two storm events.

At the study site, we deployed a sawhorse frame with two Nortek acoustic Doppler velocimeters (ADVs), placed with their measurement volumes at 5 and 15 cm above the bed (cmab), respectively. Each ADV sampled the 3-D velocity and pressure at 8 Hz for 14 min each hour. On the same platform, we deployed a Nortek Vectrino Profiler (Vectrino) with its measurement volume overlapping the bed. The Vectrino sampled the 3-D velocity at 64 Hz over fifteen 1 mm-spaced vertical bins situated from 0–1.5 cmab. The Vectrino logged in 12 and 14 min bursts each hour during summer and spring, respectively. Due to a battery failure, the Vectrino did not log during winter. We also deployed an upward-facing Nortek Aquadopp acoustic Doppler current profiler (ADP) on an auxiliary plate 10 m from the ADVs. The ADP reported velocity profiles over 0.1 m bins every 3 min based on 72 s of sampling.

In addition to moored instruments, we collected two sediment cores for an erosion study duringsummer. Each core contained hundreds of feeding tubes built by *Sabaco elongatus* and *Ampelisca abdita* (a benthic worm and amphipod, respectively), which significantly altered the structure of the near-bed flow (see Egan et al., 2019, for a sediment core image). To obtain high-resolution images of the sediment bed and better characterize the benthic canopy structure, we conducted Sediment Profile Imaging (SPI) during winter and spring (Germano et al., 2011; Rhoads & Cande, 1971). The SPI system consisted of a Nikon D7100 digital single-lens reflex camera with a 24.1-megapixel image sensor mounted inside an Ocean Imaging Model 3731 pressure housing system. Images were collected adjacent to the study site, with 11 images collected in winter and 19 in spring. Each image provided a 14.5×21 cm^2 profile view of the sediment-water interface.

3. Data Processing Methods

The major and minor directions of the tidal ellipse were estimated from the first and second principal components of the depth-averaged (below 100 cmab to avoid wave contamination) ADP mean velocity timeseries

(Figure 1). The ADV and Vectrino data were rotated into those coordinate systems for each deployment. We denote the major velocity component u, the minor component v, and the vertical component w. Because the flow was both wave- and current-driven, each velocity component can be decomposed as

$$u = \bar{u} + \tilde{u} + u', \tag{3}$$

where $\bar{u}$ is the burst period-averaged velocity, $\tilde{u}$ is the wave velocity, and u' is the turbulent fluctuating velocity. Assuming that waves and turbulence are uncorrelated (i.e., terms like $\overline{u'\tilde{w}}$ vanish), the total vertical momentum flux can be decomposed into a turbulent and wave component,

$$\overline{uw} = \overline{u'w'} + \overline{\tilde{u}\tilde{w}}, \tag{4}$$

where $\overline{u'w'}$ is the turbulent Reynolds stress and $\overline{\tilde{u}\tilde{w}}$ is the wave momentum flux. This decomposition was performed with the phase method (Bricker & Monismith, 2007).

The drag coefficient was calculated following Fong et al. (2009). Rearranging Equation 2 and setting $\tau_b \rho_0^{-1} = -\overline{u'w'}$, we obtain

$$C_D = \frac{-\overline{u'w'}}{\bar{u}|\bar{u}|}. \tag{5}$$

The drag coefficient is then estimated as the best-fit slope from a least squares regression of $-\overline{u'w'}$ as a function of $\bar{u}|\bar{u}|$. Retaining the sign of $\bar{u}|\bar{u}|$, this produces a C_D value for both flood and ebb tide. Though it is common to use the reference velocity at 100 cmab in Equation 5 (Dronkers, 1964), our ADP measurements at that height were relatively noisy. Therefore, we used the 15 cmab ADV timeseries of $\bar{u}|\bar{u}|$ for all C_D estimations. For the Vectrino data, we vertically averaged the Reynolds stress from 0.5–1 cmab because this corresponds to the region of highest signal-to-noise ratio over the profile (Koca et al., 2017). Assuming that the flow follows the law of the wall (Schlichting & Gersten, 2016), we can calculate the bottom roughness, z_0, in terms of C_D as

$$z_0 = \frac{z_r}{\exp\left(\frac{\kappa}{\sqrt{C_D}}\right)}, \tag{6}$$

where $z_r = 15$ cm is the reference height and κ is the von Kármán coefficient. While our analysis will focus primarily on C_D, we will also report z_0 values.

Wave statistics were estimated from 15 cmab ADV data. The mean wave direction for each burst was calculated following Herbers et al. (1999), and the wave frequency, ω, was estimated from the peak in the horizontal velocity power spectrum. The bottom wave-orbital velocity, u_b, was estimated as

$$u_b = \sqrt{2\mathrm{var}(u_w')}, \tag{7}$$

where $u_w' = u_w - \bar{u}_w$ is the fluctuating velocity in the dominant wave direction (Wiberg & Sherwood, 2008).

SPI image analysis was conducted using Integral Consulting Inc.'s MATLAB-based software, iSPI v1.1 (Revelas et al., 2018). The relevant measured parameter was number of surface feeding tubes.

4. Results

Figures 2a and 2b show C_D and z_0 estimated from Vectrino data for summer and spring, respectively. The most striking difference between the two deployments is that the summer drag coefficient was approximately twice as large as the spring drag coefficient on ebb tide. From Equation 5, this can be attributed to suppressed $\bar{u}|\bar{u}|$ in summer, the maximum magnitude of which was approximately half of that during spring. Though tide gage data from a nearby station (NOAA 9414523) showed no significant seasonal difference in the phase-averaged tidal height (not shown), the ADP tidal ellipses (Figure 1) did show reduced summer velocities. This suggests that the suppressed velocities were caused by a local roughness increase upstream

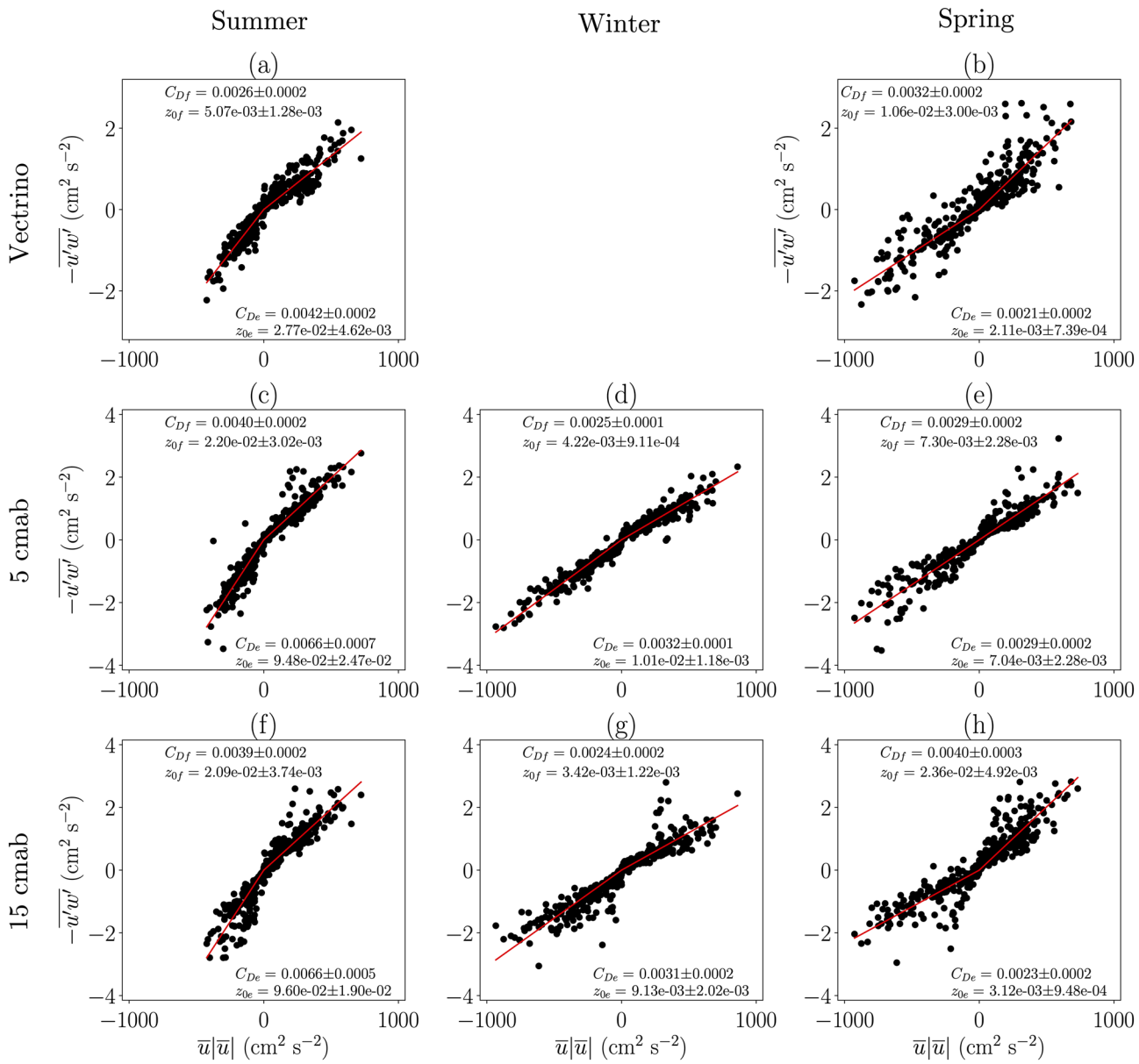

Figure 2. Turbulent Reynolds stress measured by the (a–b) Vectrino, vertically averaged from 0.5–1 cmab, (c–e) 5 cmab ADV, and (f–h) 15 cmab ADV, as a function of the 15 cmab ADV squared velocity magnitude for the (a, c, f) summer, (d, g) winter, and (b, e, h) spring. The best fit lines are shown in red, with the slopes indicating the drag coefficients for ebb tide (C_{De}, bottom) and flood tide (C_{Df}, top). The bottom roughness (z_0, cm) was calculated with Equation 6. Error bounds are bootstrapped 95% confidence intervals.

of the study site on ebb tide, rather than reduced tidal forcing. The flood tide C_D was not affected in the same manner; instead, it was slightly larger during spring.

The Vectrino sampled within the boundary layer among the roughness elements. Therefore, its drag estimates may be particularly sensitive to changes in bed characteristics. To examine whether the Vectrino estimates are consistent with those derived from measurements taken further from the bed, Figures 2c–2e and 2f–2h show the drag coefficients estimated by ADVs at 5 and 15 cmab, respectively.

The drag coefficients calculated by the two ADVs generally agreed, with all but two falling within the error bounds of each other. They also showed the same trend as the Vectrino drag coefficients, with larger ebb tide drag in summer compared to spring by up to a factor of three. The ADV drag coefficients were also reduced

during winter, though there is no Vectrino data for comparison. In terms of magnitude, the spring drag coefficients for the Vectrino and ADVs were much closer to each other than they were in summer, when the Vectrino drag coefficients were all significantly smaller than the ADV estimates.

Both the sediment cores collected in summer and the SPI surveys in winter and spring provided profile images of the sediment water interface. Therefore, for each collection method we counted the visible feeding tubes in each image and converted the number of tubes into a linear density. For the summer cores, this resulted in 344 surface tubes per meter. From the winter and spring SPI images, we found averages of only 62 and 68 tubes per meter, respectively. This decrease by approximately a factor of five indicates that the feeding tube canopies were far denser during summer than they were during winter and spring. The heights of the feeding tubes also varied seasonally. In summer, the tubes ranged from 0.5–1.5 cm. The few tubes that were observed in winter were taller, ranging from 1 to 2 cm. In spring, most tubes were smaller (0–0.5 cm), though three images contained ≈1 cm tubes.

Given roughness element length scales k_b, the bed can be classified as hydraulically rough or smooth by calculating $z_0^+ = u_* k_b/\nu$, where $u_* = \left|\overline{u'w'}\right|^{1/2}$ is the friction velocity and ν is the kinematic viscosity. For summer, we measured an average $u_* = 0.8$ cm s^{-1}, so using $k_b = 1$ cm results in $z_0^+ = 80$, which is considered hydraulically rough (Nielsen, 1992). This is consistent with the summer z_0 values in Figure 2, which are expected to follow $z_0 = k_b/30$ for a rough bed. For a smooth bed, z_0 is given by $z_0 = \frac{1}{9}\nu/u_*$. Using the same u_* as above, we find $z_0 =$ 1.39e-3 cm, which is generally smaller than the Figure 2 winter and spring z_0 values. However, using $k_b = 1$ cm for winter and spring would result in vast overestimates of z_0 compared to Figure 2, indicating that the proper roughness height during those seasons falls somewhere between the sediment grain size (≈ 10 μm) and the height of the sparse roughness elements ($\approx$ 0.1–1 cm).

5. Discussion

Bottom drag variability can generally be attributed to wave and roughness variability; each of these factors can be examined using the Grant and Madsen (1979) model (hereafter GM1979), which estimates combined wave-current bottom drag. GM1979 takes as input the bottom wave-orbital velocity, u_b; the current velocity, u_r, at a reference height $z = z_r$, which we chose as $z_r = 15$ cmab; the wave frequency, ω; the physical bottom roughness, k_b; and the angle between the waves and currents, ϕ_{wc}. The mean values and 95% confidence intervals for each parameter during each deployment are listed in Table 1. For k_b, we estimated the summer value as 1 cm, the approximate height of the sediment core feeding tubes. For winter and spring, we assumed $k_b = 0.1$ cm due to the observed decrease in canopy density during the SPI survey.

From the model, we calculated the drag coefficient $C_D = u_{*c}^2 u_r^{-2}$, where u_{*c} is the current shear stress as influenced by the waves. We also report the apparent bottom roughness, z_{0a}, which the model calculates directly. These quantities can be compared to our measured C_D and z_0 because they are also influenced by both waves and roughness. Given a constant turbulent stress, the addition of waves to a current decreases the time-averaged near-bed velocity (Nielsen, 1992), thus increasing the drag coefficient (Equation 5) and associated bottom roughness (Equation 6). Using the mean parameter values for each season resulted in modeled C_D (and z_{0a}) estimates of $C_D = 0.008$ ($z_{0a} =$ 1.53e-1 cm), $C_D = 0.0031$ ($z_{0a} =$ 9.60e-3 cm), and $C_D = 0.0036$ ($z_{0a} =$ 1.62e-2 cm) for summer, winter, and spring, respectively. While these values are slightly higher than those observed in Figure 2, they track the seasonal trend and indicate that our roughness inputs are reasonable.

To isolate the effect of an individual parameter on the bottom drag, we first calculated a baseline drag coefficient, C_{Dsum}, from the mean summer value of each parameter. We then varied each parameter individually from its summer value to its winter and spring values, while holding all other parameters constant at their summer values. This allowed for estimation of two ratios for each parameter, $C_{Dsum}(C_{Dwin})^{-1}$ and $C_{Dsum}\left(C_{Dspr}\right)^{-1}$, the factors by which the summer drag coefficient would increase over the winter and spring drag coefficients, respectively, based on the seasonal change in each parameter. The same procedure was applied to the apparent bottom roughness. The uncertainty estimates for each ratio are the maximum deviations (upward and downward) from the mean ratio after sweeping the input parameter across its 95%

Table 1
Seasonal Averages and 95% Confidence Intervals (Summer, Winter, and Spring) for Each of the GM1979 Input Parameters: The Bottom Wave-Orbital Velocity (u_b, cm s^{-1}), Mean Reference Velocity at 15 cmab (u_r, cm s^{-1}), Wave Frequency (ω, rad s^{-1}), Nikuradse Roughness (k_b, cm), and Angle Between the Waves and Currents (ϕ_{wc}, degrees)

Variable	Seasonal averages	$C_{Dsum}(C_{Dwin})^{-1}$	$C_{Dsum}(C_{Dspr})^{-1}$
u_b	$(6.57 \pm 0.32,\ 3.66 \pm 0.21,\ 5.79 \pm 0.40)$	$1.18^{+0.04}_{-0.04}\left[1.49^{+0.11}_{-0.10}\right]$	$1.04^{+0.04}_{-0.04}\left[1.09^{+0.10}_{-0.09}\right]$
u_r	$(11.21 \pm 0.59,\ 13.64 \pm 0.69,\ 13.75 \pm 0.70)$	$1.08^{+0.05}_{-0.04}\left[1.20^{+0.12}_{-0.11}\right]$	$1.08^{+0.05}_{-0.04}\left[1.21^{+0.12}_{-0.11}\right]$
ω	$(2.24 \pm 0.06,\ 1.33 \pm 0.08,\ 1.94 \pm 0.08)$	$1.05^{+0.01}_{-0.01}\left[1.12^{+0.02}_{-0.02}\right]$	$1.01^{+0.01}_{-0.01}\left[1.03^{+0.02}_{-0.02}\right]$
k_b	$(1 \pm 0.1,\ 0.1 \pm 0.05,\ 0.1 \pm 0.05)$	$2.01^{+0.86}_{-0.63}\left[6.83^{+11.26}_{-4.30}\right]$	$2.01^{+0.86}_{-0.63}\left[6.83^{+11.26}_{-4.30}\right]$
φ_{wc}	$(28.21 \pm 3.38,\ 35.08 \pm 7.21,\ 15.88 \pm 3.80)$	$1.01^{+0.01}_{-0.01}\left[1.01^{+0.02}_{-0.02}\right]$	$0.99^{+0.01}_{-0.01}\left[0.98^{+0.01}_{-0.01}\right]$

Note. $C_{Dsum}(C_{Dwin})^{-1}$ is the factor by which the drag coefficient would increase after changing the parameter from its winter to summer value, with all other parameters fixed. $C_{Dsum}(C_{Dspr})^{-1}$ is the analogous factor for spring. The values in square brackets are the corresponding ratios of apparent bottom roughness, $z_{0asum}(z_{0awin})^{-1}$ and $z_{0asum}(z_{0aspr})^{-1}$.

confidence interval. Because the model is nonlinear, the uncertainty is asymmetric and the ratios are reported as $R^{+\alpha_1}_{-\alpha_2}$, where R is the mean ratio, $R{+}\alpha_1$ is the maximum ratio, and $R{-}\alpha_2$ is the minimum ratio.

From this analysis, we found that seasonal variability in ω and φ_{wc} would not be expected to alter C_D by more than a few percent (Table 1). Increased u_b in summer relative to winter could increase C_D by 18%, potentially explaining some of the increase in Figure 2. This trend, however, is not apparent in spring: Despite much stronger waves than winter, the drag coefficients do not change significantly. These results suggest that variations in wave frequency, direction, and magnitude cannot on their own explain the increased bottom drag measured during summer.

Given that waves alone cannot account for a factor of 2–3 increase in C_D, we can next quantify the effect of roughness. Changing k_b from 0.1 to 1 cm, C_D increases by a factor of 2.01, a much greater proportion than any of the wave effects. And if, as we hypothesize, the increased roughness decreased the mean velocity at our study site that can increase drag by an additional 8%. This suggests that the measured drag increases were likely caused by seasonal variations in bottom roughness, rather than wave conditions. This conclusion is also supported by the benthic surveys, which found far fewer surface feeding tubes during winter and spring than in summer.

Any appreciable change in bed characteristics between summer and spring under fixed tidal forcing (as indicated by no apparent difference in water levels) should also be apparent in the near-bed mean velocity. Plotted in Figure 3a are profiles of mean velocity measured by the Vectrino and ADVs for both summer and spring, separated by flood and ebb tide, and averaged across their respective deployments.

The first difference between the two deployments is that the near-bed velocity is more suppressed in summer compared to spring, which is expected given the dense feeding tube canopy. Further from the bed, the summer velocity profile takes the hyperbolic tangent form classically found in canopy flows, as discussed in Egan et al. (2019). These effects are less pronounced in spring, when the velocity profile is nearly linear with height. This profile is qualitatively similar to velocity profiles measured within sparser, inhomogeneous canopies, where the inflection point in the hyperbolic tangent profile disappears (Finnigan, 2000). The ADV velocity measurements also differ across seasons: The summer ebb tide velocity is significantly suppressed at both 5 and 15 cmab.

Turbulence statistics also varied seasonally, as shown in Figure 3b. During spring, the Reynolds stress was greater in magnitude over the Vectrino profile for both flood and ebb tide. At 5 and 15 cmab, the differences were not as significant. For a constant mean current magnitude, the increase in near-bed Reynolds stress magnitude during spring would increase drag (Equation 5). However, the mean velocity magnitude increased by a greater factor than the Reynolds stress, leading to a net drag decrease.

Another impact of the rough bed during summer was a strong near-bed wave momentum flux, $\widetilde{\widetilde{u}\widetilde{w}}$ (Egan et al., 2019). If roughness was reduced in spring, we would expect a corresponding reduction in the magnitude of $\widetilde{\widetilde{u}\widetilde{w}}$. This is precisely what we see in Figure 3c, which shows deployment-averaged profiles

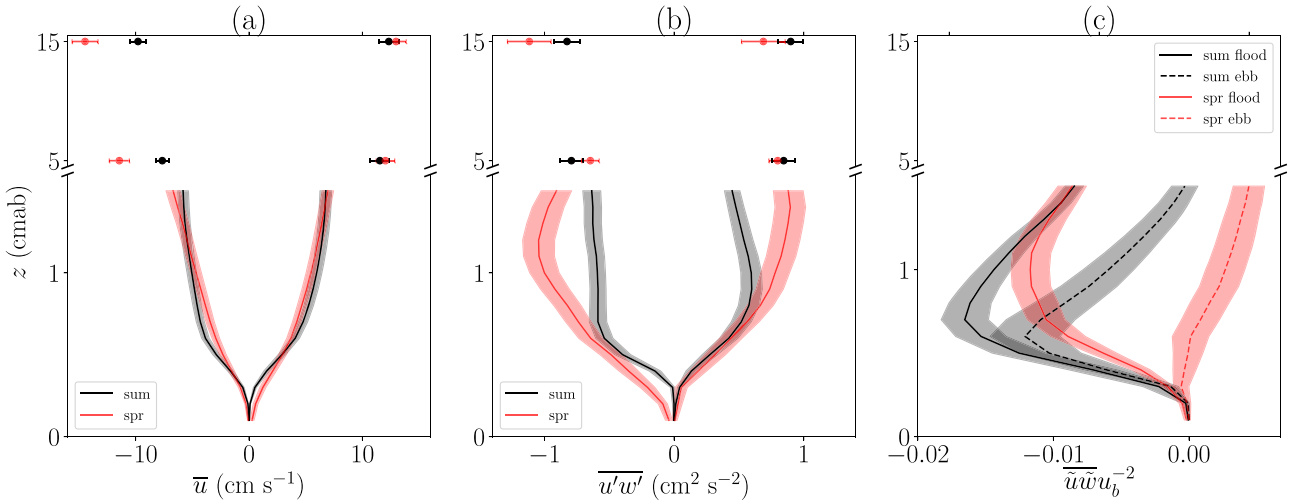

Figure 3. Profiles during summer (black) and spring (red) of the (a) mean velocity, with flood tide positive and ebb tide negative, (b) turbulent Reynolds stress, with flood tide negative and ebb tide positive, and (c) wave momentum flux, normalized by u_b^2, with flood tide denoted by solid lines and ebb tide by dashed lines. Panels (a) and (b) show ADV data at 5 and 15 cmab. The 95% confidence intervals are denoted by error bars for the ADV, and shaded regions for the Vectrino.

of $\tilde{\tilde{u}}\tilde{\tilde{w}}u_b^{-2}$ for both Vectrino deployments. Here, we normalize by u_b^2 to account for wave strength variations between deployments.

For both summer and spring, $\tilde{\tilde{u}}\tilde{\tilde{w}}u_b^{-2}$ is substantially larger in magnitude during flood compared to ebb tide. This could be due to the approximate alignment of the waves with currents during flood, contrasting with ebb when they are in opposition. For either tidal direction, however, the wave momentum flux is much smaller in magnitude in spring relative to summer. Presumably, the smoother bed cannot generate as much vorticity as the rough canopy, and vorticity generation is required to break the orthogonality between the vertical and horizontal wave velocity components and induce a nonzero $\tilde{u}\tilde{w}$. This result is consistent with other field studies (Nayak et al., 2015) and numerical simulations of wave boundary layer flow (Holmedal & Myrhaug, 2009).

Comparing drag coefficients between the Vectrino and ADVs, we find that their estimates vary significantly in summer but are closer to each other in spring. If the bed was smoother and more uniform during spring, it follows that the Vectrino and ADV estimates would agree. Furthermore, the fact that the Vectrino Reynolds stresses were generally lower than the ADV stresses in summer implies a rougher, more heterogeneous bed because either (a) Vectrino-measured turbulent fluctuations are damped near the canopy (consistent with Figure 3b) or (b) the Vectrino was deployed above a section of the bed where the canopy was slightly less dense than average. Therefore, the ADV measurements were arguably more representative of the large-scale, integrated roughness characteristics, giving a more reliable bulk estimate of the bottom drag.

Differences between the two measurement techniques imply that increased roughness is more likely than waves to be responsible for increasing the bottom drag during summer. This hypothesis is consistent with the GM1979 analysis (Table 1), the vertical structure of the Vectrino mean velocity (Figure 3a), the increased wave momentum flux over the roughness elements during summer (Figure 3c), the reduced mean velocities measured by the ADV (Figure 2) and ADP (Figure 1), and the abundance of feeding tubes observed in sediment bed images collected in summer compared to winter and spring. These results are also consistent with recent studies in the region, where it was found that bottom roughness was enhanced in summer relative to winter (Allen et al., 2019; Lacy & MacVean, 2016). And although our benthic surveys were far from comprehensive, previous studies over the shoals of San Francisco Bay found that *Ampelisca abdita* populations peak in summer and fall and decline in winter and spring as salinity decreases during the rainy season (Nichols & Thompson, 1985).

6. Conclusion

Compared to winter and spring, the ADV-derived drag coefficients in summer were larger by up to a factor of three. If this increase is, as we hypothesize, caused by seasonal variations in benthic biology, the implications for hydrodynamic modeling are troubling. While recent modeling efforts have allowed for spatially varying bottom roughness (e.g., Ralston et al., 2017), they do so using an optimization framework because it is financially infeasible to survey spatiotemporal roughness patch variability across an entire estuary. Yet optimizing for bottom roughness also requires long-term high-resolution field data for validation, and such a procedure would likely smooth over some amount of small-scale variability. As we showed here, those deviations can profoundly affect the local bottom drag, and any discrepancy in C_D could further affect estimates of sediment transport, estuarine residence time, or nutrient fluxes.

These results, though based on measurements in San Francisco Bay, could be applicable to other estuarine systems. Of the two species that we sampled, *Sabaco elongatus* has a native range in the western Atlantic from the Gulf of St. Lawrence to Belize and is distributed in the eastern Pacific from Canada to Mexico (Hughes & Thomas, 1971; Light, 1974). *Ampelisca abdita* is similarly distributed across both the eastern and western seaboards of the United States (Bousfield, 1973), suggesting that bottom drag could be affected by living roughness elements in estuaries across North America.

We hope that these results inspire both further studies into the effects of small-scale benthic biology on large-scale hydrodynamics and increased communication between estuarine hydrodynamic modelers and biologists. Even coarse estimates of benthic population density across seasons and sub-embayments could help inform drag coefficient estimates. This approach could be a major improvement over treating bottom roughness as a tuning parameter and would be a step forward in the development of purely physics-based hydrodynamic models.

Data Availability Statement

All field data used in this paper are available at https://purl.stanford.edu/wv787xr0534 and the benthic survey images are available online (https://purl.stanford.edu/sh883gp0753).

Acknowledgments
This work was funded by the US National Science Foundation under grant OCE-1736668. We thank Frank Spada, Kara Scheu, Craig Jones, Sam McWilliams, Marianne Cowherd, Stephen LaMothe, and Jim Christmann for their assistance with the field work. We also thank the two anonymous reviewers whose suggestions improved the quality of this manuscript.

References

Allen, R. M., Lacy, J. R., Stacey, M. T., & Variano, E. A. (2019). Seasonal, Spring-Neap, and tidal variation in cohesive sediment transport parameters in estuarine shallows. *Journal of Geophysical Research: Oceans*, *124*, 7265–7284. https://doi.org/10.1029/2018JC014825

Bousfield, E. L. (1973). *Shallow-water gammaridean Amphipoda of New England*. Comstock Publishing Associates.

Bricker, J. D., & Monismith, S. G. (2007). Spectral wave–turbulence decomposition. *Journal of Atmospheric and Oceanic Technology*, *24*(8), 1479–1487.

Dronkers, J. J. (1964). *Tidal computations in rivers and coastal waters*. North-Holland publishing company Amsterdam.

Egan, G., Cowherd, M., Fringer, O., & Monismith, S. (2019). Observations of near-bed shear stress in a shallow, wave-and current-driven flow. *Journal of Geophysical Research: Oceans*, *124*, 6323–6344. https://doi.org/10.1029/2019JC015165

Egbert, G. D., & Erofeeva, S. Y. (2002). Efficient inverse modeling of barotropic ocean tides. *Journal of Atmospheric and Oceanic Technology*, *19*(2), 183–204.

Finnigan, J. (2000). Turbulence in plant canopies. *Annual Review of Fluid Mechanics*, *32*(1), 519–571.

Fong, D. A., Monismith, S. G., Stacey, M. T., & Burau, J. R. (2009). Turbulent stresses and secondary currents in a tidal-forced channel with significant curvature and asymmetric bed forms. *Journal of Hydraulic Engineering*, *135*(3), 198–208.

Fringer, O. B., Dawson, C. N., He, R., Ralston, D. K., & Zhang, Y. J. (2019). The future of coastal and estuarine modeling: Findings from a workshop. *Ocean Modelling*, *143*, 101458.

Germano, J. D., Rhoads, D. C., Valente, R. M., Carey, D. A., & Solan, M. (2011). The use of sediment profile imaging (SPI) for environmental impact assessments and monitoring studies: Lessons learned from the past four decades. *Oceanography and Marine Biology: An Annual Review*, *49*, 235–298.

Geyer, W. R., Trowbridge, J. H., & Bowen, M. M. (2000). The dynamics of a partially mixed estuary. *Journal of Physical Oceanography*, *30*(8), 2035–2048.

Grant, W. D., & Madsen, O. S. (1979). Combined wave and current interaction with a rough bottom. *Journal of Geophysical Research*, *84*(C4), 1797–1808.

Herbers, T. H. C., Elgar, S., & Guza, R. T. (1999). Directional spreading of waves in the nearshore. *Journal of Geophysical Research*, *104*(C4), 7683–7693.

Holmedal, L. E., & Myrhaug, D. (2009). Wave-induced steady streaming, mass transport and net sediment transport in rough turbulent ocean bottom boundary layers. *Continental Shelf Research*, *29*(7), 911–926.

Hughes, R. N., & Thomas, M. L. H. (1971). The classification and ordination of shallow-water benthic samples from Prince Edward Island, Canada. *Journal of Experimental Marine Biology and Ecology*, *7*(1), 1–39.

Koca, K., Noss, C., Anlanger, C., Brand, A., & Lorke, A. (2017). Performance of the vectrino profiler at the sediment–water interface. *Journal of Hydraulic Research*, *55*(4), 573–581.

Lacy, J. R., & MacVean, L. J. (2016). Wave attenuation in the shallows of San Francisco Bay. *Coastal Engineering*, *114*, 159–168.

Light, W. (1974). Occurrence of the Atlantic maldanid Asychis elongata (Annelida, Polychaeta) in San Francisco Bay, with comments on its synonymy. *Proceedings of the Biological Society of Washington*, *87*, 175.

Longuet-Higgins, M. S. (1970). Longshore currents generated by obliquely incident sea waves: 1. *Journal of Geophysical Research*, *75*(33), 6778–6789.

Nayak, A. R., Li, C., Kiani, B. T., & Katz, J. (2015). On the wave and current interaction with a rippled seabed in the coastal ocean bottom boundary layer. *Journal of Geophysical Research: Oceans*, *120*, 4595–4624. https://doi.org/10.1002/2014JC010606

Nichols, F. H., & Thompson, J. K. (1985). Time scales of change in the San Francisco Bay benthos, *Temporal dynamics of an estuary: San Francisco Bay* (pp. 121–138). Springer.

Nielsen, P. (1992). *Coastal bottom boundary layers and sediment transport* (Vol. 4). World scientific.

Pawlowicz, R., Beardsley, B., & Lentz, S. (2002). Classical tidal harmonic analysis including error estimates in MATLAB using t_tide. *Computers & Geosciences*, *28*(8), 929–937.

Ralston, D. K., Cowles, G. W., Geyer, W. R., & Holleman, R. C. (2017). Turbulent and numerical mixing in a salt wedge estuary: Dependence on grid resolution, bottom roughness, and turbulence closure. *Journal of Geophysical Research: Oceans*, *122*, 692–712. https://doi.org/10.1002/2016JC011738

Revelas, E., Sackmann, B., Thurlow, A., Jones, C. (2018). Mapping benthic habitat conditions and seafloor deposits using sediment profile imaging and a semiautomated image processing system. In *Offshore Technology Conference*. Offshore Technology Conference.

Rhoads, D. C., & Cande, S. (1971). Sediment profile camera for in situ study of organism-sediment relations 1. *Limnology and Oceanography*, *16*(1), 110–114.

Schlichting, H., & Gersten, K. (2016). *Boundary-layer theory*. Springer.

Styles, R., & Glenn, S. M. (2000). Modeling stratified wave and current bottom boundary layers on the continental shelf. *Journal of Geophysical Research*, *105*(C10), 24,119–24,139.

Trowbridge, J. H., & Lentz, S. J. (2018). The bottom boundary layer. *Annual Review of Marine Science*, *10*, 397–420.

Wiberg, P. L., & Sherwood, C. R. (2008). Calculating wave-generated bottom orbital velocities from surface-wave parameters. *Computers & Geosciences*, *34*(10), 1243–1262.